# Harvesting waste heat produced in solid oxide fuel cell using near-field thermophotovoltaic cell

Tianjun Liao [a,b], Qijiao He [a], Qidong Xu [a], Yawen Dai [a], Chun Cheng [a], Meng Ni [a,*]

[a] Department of Building and Real Estate, The Hong Kong Polytechnic University, Hung Hom, Kowloon, Hong Kong, China
[b] Department of Physics and Energy, Chongqing University of Technology, Chongqing, 400054, China

## HIGHLIGHTS

- A coupled system integrating NFTC with SOFC can increase power output density.
- The area matching between the two sub-cells is given based on energy balance.
- The parametric optimal working regions are given by comparing to the single SOFC.
- The effects of NFTC's vacuum gap and SOFC′ temperature on the system are analyzed.
- The proposed model and the other SOFC-based coupled systems are compared.

## ARTICLE INFO

## ABSTRACT

A coupled system consisting of a regenerator, a solid oxide fuel cell (SOFC), and a near-field thermophotovoltaic cell (NFTC) is proposed to recovery the waste heat from the SOFC. Based on the theories of electrochemical and fluctuation electrodynamics, analytical formulas for the power output and the energy efficiency of the coupled system are derived. The dependence of the matching area ratio between the subsystems on the key parameters is discussed. As the SOFC works at 1073 K, the two voltages of the subsystems are optimized. The maximum power output density of 1.01 $Wcm^{-2}$ and an efficiency of 0.402 are achieved for the proposed system. By comparing to the performance of the single SOFC, the optimally working regions of the coupled system are determined. The effects of the SOFC's temperature and the NFTC's vacuum gap on the maximum power output density and the optimum operating conditions of the system are studied. One can find that the maximum power density in the near-field is 1.3 times than that in the far-field and better than the most of the other SOFC-based systems. The present work can provide a new route to efficiently utilize the waste heat of SOFC to achieve higher energy efficiency.

## 1. Introduction

Solid oxide fuel cell (SOFC) is a solid-state power device that converts chemical energy of a fuel into electricity [1]. The SOFCs have attracted tremendous attention due to their high efficiency, low noise, safety, low pollution etc. [2–5]. As SOFCs work at a high temperature such as 800 °C, the waste heat from the SOFC stack is of high quality and can be recovered by integrating SOFC stacks with other thermal-to-power energy conversion devices to increase the overall energy efficiency of the coupled system. Zhao et al. [6] proposed and modeled an SOFC-Carnot heat engine coupled system. The overall thermodynamic performances of the coupled system were optimized,

and the optimal operating regions of some key parameters of the system were given. Chen et al. [7] studied and evaluated the SOFC-single stage thermoelectric generator (STEG) coupled system. The results showed that the coupled system could efficiently harness the waste heat. Making a trade-off between the power output density and efficiency, the parametric optimal operating regions were given. Zhang et al. [8] proposed a method to harness the waste heat in the SOFC based on the two stage-thermoelectric generators (TTEG). The maximum power output density and energy conversion efficiency of the coupled system were determined. The results showed that the TTEG-based coupled system is superior to the STEG-based coupled system only when the SOFC operates at high temperature. Wang et al. [9] applied thermionic generator (TIC) to recycle the waste heat in the SOFC. The high work function of

---

## Nomenclature

| | |
|---|---|
| $A$ | area $(cm^{-2})$ |
| $c$ | speed of light $(cms^{-1})$ |
| $d$ | vacuum gap (nm) |
| $e$ | elementary positive charge (C) |
| $F$ | Faraday's constant $(C\,mol^{-1})$ |
| $\Delta g$ | molar Gibbs energy $(Jmol^{-1})$ |
| $\hbar$ | reduced Planck constant (Js) |
| $-\Delta h$ | molar enthalpy change $(J\,mol^{-1})$ |
| $-\Delta \dot{H}$ | enthalpy change (J) |
| $J$ | current density $(Acm^{-2})$ |
| $J_{e,a}$ | exchange current density of anode $(Acm^{-2})$ |
| $J_{e,c}$ | exchange current density of cathode $(Acm^{-2})$ |
| $J_{L,a}$ | limiting current density of anode $(Acm^{-2})$ |
| $J_{L,c}$ | limiting current density of cathode $(Acm^{-2})$ |
| $K$ | Boltzmann constant $(JK^{-1})$ |
| $k$ | wave vector $(cm^{-1})$ |
| $L_{et}$ | electrolyte thickness (cm) |
| $N$ | number of electrons transferred in reaction |
| $n$ | refraction index |
| $P$ | power output (W) |
| $P^*$ | power density of coupled system $(Wcm^{-2})$ |
| $p_i$ | partial pressure (atm) |
| $q_j$ | heat flow (W) |
| $r$ | Fresnel's coefficients |
| $R$ | universal gas constant $(J\,mol^{-1}K^{-1})$ |
| $s$ | coupling coefficient $(cm^{-1})$ |
| $T$ | temperature (K) |
| $U$ | heat transfer coefficient $(Wcm^{-2}K^{-4})$ |
| $V$ | voltage (V) |
| $W_{ae}$ | activation energy for ion transport $(J\,mol^{-1})$ |
| $E$ | photon energy (J) |
| $E_g$ | PV cell bandgap (J) |
| $E_c$ | energy level at the bottom of conduction band (J) |
| $E_v$ | energy level at the top of valence band (J) |
| $E_{fe}$ | quasi-Fermi level of electrons (J) |
| $E_{fh}$ | quasi-Fermi level of holes (J) |
| $Z$ | objective function $(Wcm^{-2})$ |

*Greek symbols*

| | |
|---|---|
| $\alpha$ | absorption coefficient $(cm^{-1})$ |
| $\beta$ | parallel wave vector $(cm^{-1})$ |
| $\lambda_{th}$ | thermal wavelength (cm) |
| $\theta$ | angle (rad) |
| $\sigma$ | reference ionic conductivity $(S\,cm^{-1})$ |
| $\eta$ | efficiency |
| $\varepsilon$ | dielectric function $(Fcm^{-1})$ |
| $\omega$ | angular frequency $(rads^{-1})$ |
| $\omega_g$ | bandgap angular frequency $(rads^{-1})$ |
| $\varphi$ | Bose distribution |

*Subscript*

| | |
|---|---|
| A | ambient |
| F | fuel cell |
| i | H2, O2, H2O |
| j | in, out, leak |
| N | near-field |
| act | activation overpotential |
| con | concentration overpotential |
| in | input |
| lb | low bound |
| max | maximum |
| ohm | ohmic overpotential |
| P | maximum power density point |
| ub | up bound |
| R | radiator |
| Rev | reversible voltage |
| su | start-up |
| s | polarized wave |
| p | polarized wave |
| V | vacuum |

*Abbreviations*

| | |
|---|---|
| BSR | back surface reflector |
| PV | photovoltaic |
| NFTC | near-field thermophotovoltaic cell |
| FFTC | far-field thermophotovoltaic cell |
| SOFC | solid oxide fuel cell |
| Evan | evanescent |
| Prop | propagating |
| FDT | fluctuation dissipation theorem |
| NFRHT | near-field radiative heat transfer |

the anode limits the power output density of the TIC. The temperature of the anode is set to 600 K due to the black-body radiation and the emission of electrons within the TIC. The above-mentioned factors lead that the maximum power output density of the TIC-based coupled system is smaller than that of the TEG-based coupled systems. In addition, the SOFC can be integrated with gas turbine [10], Braysson [11], and Brayton [12] heat engines and Rankine cycle [13] to recovery its waste heat. Although the performances of above four types systems are superior to the TEG- and TIC-based coupled systems, these large-scale systems with rotating parts require complex designs, which hinder the development. It is necessary to develop small coupled systems that present high performances and are easy to design. In a recent work, the far-field thermophotovoltaic cell (FFNC) was integrated with SOFC [14]. The maximum power output density was calculated. The optimal operating regions of the coupled system were determined, compared with the performance of the single SOFC. The selection criteria of some key parameters were given. The proposed model can efficiently exploit the waste heat produced in SOFC.

Especially, as the vacuum gap is far less than the characteristic wavelength of thermal radiation given by Wien's displacement law, the near-field thermophotovoltaic cell (NFTC) can efficiently convert high-grade thermal energy into electricity [15]. Based on the NFTC, the conceptual models of TIC-NFTC coupled system have been proposed to improve the thermoelectric conversion efficiency [16–18]. Therefore, it is expected that NFTC can be very promising for utilizing the waste heat of SOFC for additional power generation. However, no research work has been reported on the SOFC-NFTC coupled system yet. In order to fill this research gap, a new SOFC-NFTC coupled system is proposed and theoretically evaluated in this work. Theoretical models are developed to simulate the performances of the NFTC and SOFC. The power output and efficiency of the coupled system are analytically derived. The optimal performance characteristics of the coupled system are discussed in detail. The results are generalized for SOFCs at different operating temperatures and compared with those of other SOFC-based coupled systems.

## 2. Model description

The SOFC-NFTC coupled system composed of an SOFC, a regenerator, a photon radiator, and a PV cell, as shown in Fig. 1(a). The role of the regenerator in the coupled system is to preheat the incoming air and fuel by using the high-temperature exhaust gas of the SOFC and to ensure that the SOFC works at temperature $T_F$ [6,18]. The radiator at temperature $T_R$ and PV cell at temperature $T_N$ are, respectively, made of hexagonal Boron Nitride (h-BN) and III-V group semiconductor material InAs (band-gap 0.36 eV) [14]. It should be indicated that other III-V group semiconductor materials such as InSb, GaSb, InGaAsSb, etc, can be also selected to make the PV cell. These two basic elements in the NFTC separated by a vacuum gap $d$ can exchange radiative heat flow $q_N$. The corresponding heat exchange area is $A_N$. The SOFC and the radiator are contacted with each other through high thermal conductivity material. The intrinsic mechanism of the coupled system is that the SOFC generates power output $P_F$ and acts as the heat source of the NFTC to generate additional power output $P_N$. The SOFC releases heat-leak rate $q_L$ and heat flow $q_{in}$ into the ambient and the NTFC, respectively. The infrared photons emitted from the radiator, through the vacuum gap due to photon tunneling effect, are absorbed by the PV cell to generate electron-hole pairs inside the semiconductor, which are extracted to an external circuit to electricity. Simultaneously, the back surface of the PV cell releases the heat flow $q_{out}$ to the ambient. For the convenience of discussion, we assume that the radiator directly contacts with the SOFC and works at a fixed temperature $T_R = T_F$.

The working principle of NFTC is presented in Fig. 1(b), where $n_R$ and $n_V$ denote the refraction indexes. The PV cell is composed of p-type and n-type semiconductors. $E_c$ and $E_v$ are the energy levels at the bottom of the conduction band and top of the valence band, whose difference $(E_c - E_v)$ corresponds the band-gap $E_g$. $E_{fe}$ and $E_{fh}$ are the quasi-Fermi levels of electrons and holes, whose difference $(E_{fe} - E_{fh})$ corresponds to the voltage output $V_N$ multiplied by an elementary positive charge $e$. The photo-generated electron-hole pairs can be separated by selective contact electrodes. The electrons go through the load to output electricity. The material properties of the radiator and PV cell are described by the frequencies dependent complex dielectric functions $\varepsilon_R(\omega)$ and $\varepsilon_N(\omega)$. The thermal radiation generated by the random thermal motion of particles within an object can be described by the fluctuation dissipation theorem (FDT). By combining of the Maxwell's equations and the FDT, the fluctuational electrodynamics theory was established to computing the near-field radiative heat transfer (NFRHT). As the incident angle $\theta_i$ and the reflex angle $\theta_r$ meet the relation $\theta_i = \theta_r \geq \arcsin(n_V / n_R)$, the evanescent (Evan) waves contributed to the NFRHT are significantly enhanced under the condition that the vacuum gap $d$ is smaller than the thermal wavelength $\lambda_{th}$. Meanwhile, the propagating (Prop) waves contributed to the NFRHT should be taken into consideration as $\theta_i = \theta_r < \arcsin(n_V / n_R)$. Importantly, the fluctuational electrodynamics theory for calculating for the NFRHT between two semi-infinite plates at different temperatures was experimentally

demonstrated [19–21]. Recently, the physical model of the NFTC was theoretically and experimentally studied [22]. Therefore, the similar model can be used to discuss the problem of the optimal coupling between the SOFC and the NFTC.

### 2.1. The power output and efficiency of an SOFC

The irreversible thermodynamic model of an SOFC has demonstrated that the efficiency $\eta_F$ and the power output $P_F$ depend on the number of electrons transferred in reaction $N = 2$, the Faraday's constant $F = 9.65 \times 10^4$ C mol$^{-1}$, the universal gas constant $R = 8.314$ J mol$^{-1}$K$^{-1}$, the current density $J_F$, the operating voltage $V_F$, and the surface area of the contact electrode $A_F$ etc. The formulas for $\eta_F$ and $P_F$ are, respectively, presented as [23–28].

$$\eta_F = \frac{P_F}{-\Delta \dot{H}} \tag{1}$$

and

$$P_F = V_F J_F A_F = (V_{Rev} - V_{act} - V_{con} - V_{ohm})J_F A_F \tag{2}$$

where $-\Delta \dot{H} = -\Delta h J_F A_F /(NF)$ represents the total enthalpy change for electrochemical reaction. $\Delta h$ stands for the molar enthalpy change for electrochemical reaction. The reversible voltage $V_{Rev}$ and irreversible voltage losses including the ohmic overpotential $V_{ohm}$, concentration overpotential $V_{con}$, and activation overpotential $V_{act}$. These overpotential terms can be, respectively, expressed as [23–28].

$$V_{Rev} = \frac{RT_F}{NF} \ln \left( \frac{p_{H_2} \sqrt{p_{O_2}}}{p_{H_2O}} \right) - \frac{\Delta g(T_F)}{NF} \tag{3}$$

$$V_{ohm} = \frac{J_F L_{et} T_F}{\sigma} \exp \left( \frac{W_{ae}}{RT_F} \right) \tag{4}$$

$$V_{con} = -\frac{RT_F}{NF} [\ln(1 - J_F / J_{L,a}) + \ln(1 - J_F / J_{L,c})] \tag{5}$$

and

$$V_{act} = \frac{2RT_F}{F} \left[ \sinh^{-1}(0.5J_F / J_{e,a}) + \sinh^{-1}(0.5J_F / J_{e,c}) \right] \tag{6}$$

where $\Delta g(T_F)$ means the molar Gibbs energy change under the standard atmospheric pressure. $p_{H_2}$, $p_{O_2}$, and $p_{H_2O}$ are, respectively, the partial pressures of the hydrogen, oxygen, and water. $J_{e,a}$ and $J_{e,c}$ are, respectively, the exchange current densities of the anode and cathode. $J_{L,a}$ and $J_{L,c}$ represent the limiting current densities of the anode and cathode. $L_{et}$, $W_{ae}$, and $\sigma$ are, respectively, the electrolyte thickness, the activation energy for ion transport and the reference ionic conductivity. The performance parameters of the SOFC are listed in Table 1.
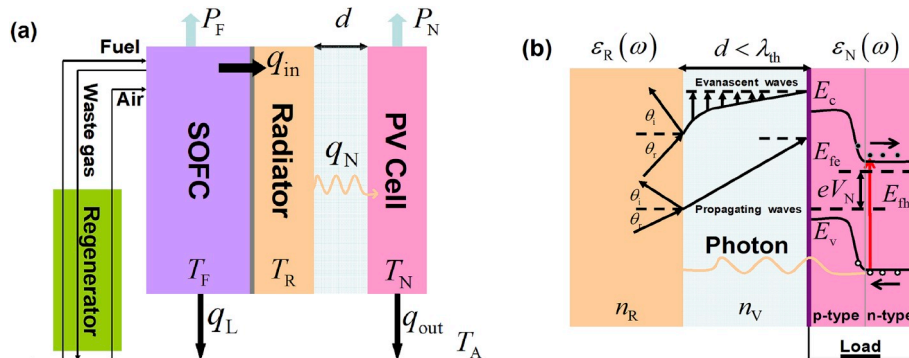


**Fig. 1.** The schematic diagram of a SOFC-NFTC coupled system and (b) the working principle of NFTC.

**Table 1**
The operating conditions and parameters of the SOFC [6,7,25].

| Parameter | Value |
|---|---|
| SOFC temperature, $T_F$ (K) | 1073 |
| Fuel composition pressures, $p_{H_2}$ (atm); $p_{H_2O}$ (atm) | 0.97; 0.03 |
| Air composition pressures, $p_{O_2}$ (atm) ; $p_{N_2}$ (atm) | 0.21; 0.79 |
| Cathode exchange current density, $J_{e,a}$(Acm$^{-2}$) | 0.53 |
| Anode exchange current density, $J_{e,c}$(Acm$^{-2}$) | 0.20 |
| Electrolyte thickness, $L_{et}$ (cm) | $2 \times 10^{-3}$ |
| Activation energy of O$^{2-}$, $W_{ae}$(J mol$^{-1}$) | $8.0 \times 10^4$ |
| Ionic conductivity of O$^{2-}$, $\sigma$(S cm$^{-1}$) | $3.6 \times 10^5$ |
| Cathode limiting current density, $J_{L,a}$ (A cm$^{-2}$) | 2.99 |
| Anode limiting current density, $J_{L,c}$(A cm$^{-2}$) | 2.16 |
| Standard molar enthalpy change at 1073 K, $\Delta h$(J mol$^{-1}$) | − 248303 |
| Standard molar Gibbs free energy change at 1073 k, $\Delta g$(J mol$^{-1}$) | − 188680 |

### 2.2. The power output of a NFTC

The two dielectric functions $\varepsilon_R(\omega)$ and $\varepsilon_N(\omega)$ of the radiator and the PV cell can be described as [15].

$$\varepsilon_R(\omega) = 4.88 \left[ \frac{\omega^2 - \left(3.032 \times 10^{14}\right)^2 + 1.001 \times 10^{12}\,\omega i}{\omega^2 - \left(2.575 \times 10^{14}\right)^2 + 1.001 \times 10^{12}\,\omega i} \right] \quad (7)$$

and

$$\varepsilon_N(\omega) = \begin{cases} n_N, & \omega < \omega_g \\ \left[ n_N + \left( ic\alpha\sqrt{\omega/\omega_g - 1}\,\right)(2\omega)^{-1} \right]^2, & \omega \geq \omega_g \end{cases} \quad (8)$$

where $n_N = 3.51$ is the refractive index of the PV cell. $\omega$ is the angular frequency. $\alpha$ is the absorption coefficient [8]. $\omega_g$ is the band-gap frequency of the PV cell. $c$ is the speed of light.

According to the fluctuation electrodynamics theory, the Prop and Evan waves in the vacuum gap generate the NFRHT flows $q_{Prop}$ and $q_{Evan}$, i.e., [19–22,29].

$$q_{Prop} = \frac{A_N}{\pi^2} \int_0^\infty \frac{d\omega}{2\pi} [\varphi(\omega, T_R) - \varphi(\omega - \omega_0, T_N)]\hbar\omega \times \int_0^{\omega/c} d\beta s_{Prop} \quad (9)$$

and

$$q_{Evan} = \frac{A_N}{\pi^2} \int_0^\infty \frac{d\omega}{2\pi} [\varphi(\omega, T_R) - \varphi(\omega - \omega_0, T_N)]\hbar\omega \times \int_{\omega/c}^\infty d\beta s_{Evan} \quad (10)$$

where the sub-band-gap photons contributed to the NFRHT is considered. The sum of $q_{Prop}$ and $q_{Evan}$ is equal to $q_N$, i.e., $q_{Evan} + q_{Prop} = q_N$. $\beta$ is the parallel wave vector component. $\varphi(\omega, T) = 1/\{\exp[\hbar\omega/(KT)] - 1\}$ is the Bose distribution. $K$ is the Boltzmann constant. $\omega_0 = 0$ means that the PV cell can't generate electron-hole pairs when $\omega < \omega_g$; $\omega_0 = V_N e/\hbar$ indicates that the PV cell can generate working voltage $V_N$. $e$ is the elementary positive charge. $\hbar$ is the reduced Planck constant. The two coupling coefficients $s_{Evan}$ and $s_{Prop}$ of evanescent waves and propagating waves can be expressed as [15,19–22,31].

$$s_{Evan} = \frac{\text{Im}(r_{R,\,p})\text{Im}(r_{N,p})\beta e^{2ik_{zV}d}}{\left|1 - r_{R,\,p} r_{N,p} e^{2ik_{zV}d}\right|^2} + \frac{\text{Im}(r_{R,s})\text{Im}(r_{N,s})\beta e^{2ik_{zV}d}}{\left|1 - r_{R,s} r_{N,s} e^{2ik_{zV}d}\right|^2} \quad (11)$$

and

$$s_{Prop} = \frac{\beta\left(1 - |r_{R,\,p}|^2\right)\left(1 - |r_{N,\,p}|^2\right)}{4\left|1 - r_{R,\,p} r_{N,p} e^{2ik_{zV}d}\right|^2} + \frac{\beta\left(1 - |r_{R,\,s}|^2\right)\left(1 - |r_{N,\,s}|^2\right)}{4\left|1 - r_{R,s} r_{N,s} e^{2ik_{zV}d}\right|^2} \quad (12)$$

where $r_{R,s} = \frac{k_{zV} - k_{zR}}{k_{zV} + k_{zR}}$, $r_{P,s} = \frac{k_{zV} - k_{zN}}{k_{zV} + k_{zN}}$, $r_{R,p} = \frac{\varepsilon_R k_{zV} - k_{zR}}{\varepsilon_R k_{zV} + k_{zR}}$, and $r_{N,p} = \frac{\varepsilon_N k_{zV} - k_{zN}}{\varepsilon_N k_{zV} + k_{zN}}$ denotes the vacuum-medium Fresnel's coefficients. The subscripts s and p

represent two polarized waves. $k_{zV} = \sqrt{(\omega/c)^2 - \beta^2}$ is the $z$ component of the wave vector in the vacuum. $k_{zR} = \sqrt{\varepsilon_R(\omega)(\omega/c)^2 - \beta^2}$ and $k_{zN} = \sqrt{\varepsilon_N(\omega)(\omega/c)^2 - \beta^2}$ are the $z$ components of the wave vectors inside the radiator and the PV cell.

When the PV cell is in operation, the current density $J_N$ is computed as [22,30,31].

$$J_N = \frac{e}{\pi^2} \int_{\omega_g}^\infty \frac{d\omega}{2\pi} [\varphi(\omega, T_R) - \varphi(\omega - \omega_0, T_N)] \left[ \int_{\omega/c}^\infty d\beta s_{Evan} + \int_0^{\omega/c} d\beta s_{Prop} \right] \quad (13)$$

Based on Eq. (13), the power output $P_N$ of the NFTC can be expressed as [22,30,31].

$$P_N = V_N J_N A_N \quad (14)$$

### 2.3. The power output and efficiency of the coupled system

According to the first law of thermodynamics, an energy balance equation is determined as

$$-\Delta\dot{H} - P_F - q_L = q_N = q_{Evan} + q_{Prop} \quad (15)$$

where $q_L = (A_F - A_N)[U(T_F^4 - T_A^4)]$ is the heat leak. $U = 2.8 \times 10^{-9}$Wcm$^{-2}$K$^{-4}$ is the effective heat transfer coefficient. Only when $-\Delta\dot{H} - P_F - q_L > 0$, the NFTC can be driven. Hence, an inequation can be derived as

$$-\Delta h J_F/(NF) - V_F J_F - (1 - A_N/A_F)\left[U(T_F^4 - T_A^4)\right] > 0 \quad (16)$$

Through numerical analysis, one can find that there exists a start-up current density $J_{F,su}$ of the SOFC. Only when $J_F > J_{F,su}$, the system can work at coupled state. On the other hand, Eq. (15) shows that three parameters $V_N$, $V_F$, and $A_F/A_N$ are coupled with each other when relevant parameters are given. Inserting Eqs. (2)-(12) into Eq. (16), $A_F/A_N$ can be determined for given two voltages $V_F$ and $V_N$.

Using Eqs. (1), (2) and (14), one can derive the power output and efficiency of the coupled system as

$$P = P_F + P_N = (V_{Rev} - V_{act} - V_{con} - V_{ohm})J_F A_F + V_N J_N A_N \quad (17)$$

and

$$\eta = \frac{P}{-\Delta\dot{H}} = \frac{(V_{Rev} - V_{act} - V_{con} - V_{ohm})J_F A_F + V_N J_N A_N}{-\Delta h J_F A_F/(NF)} \quad (18)$$

Equations (14)-(18) can be directly used to analyze the optimum performance of the coupled system.

### 3. Optimum performance analyses

Using Eqs. (15), (17) and (18), the dependences of area ratio $A_F/A_N$, the power output density $P^*$, and the efficiency $\eta$ on $V_F$ and $V_N$ can be obtained, as shown in Fig. 2. In Fig. 2(a), $A_F/A_N$ decreases with increasing $V_N$ at a given $V_F$, because the increase of $V_N$ increases the electrochemical potential $eV_N$ of the infrared photons and decreases the near-field radiative heat flow $q_N$ [32,33]. Consequently, the coupled system should decrease $A_F/A_N$ to meet the energy balance Eq. (15). Fig. 2(a) shows that $A_F/A_N$ increases with increasing $V_F$ at a given $V_N$, because the increase of $V_N$ decreases the waste heat flow $(-\Delta\dot{H} - P_F)$, and thus, the coupled system should increase $A_F/A_N$ to meet the energy balance Eq. (15). One can find from Fig. 2(b) that the voltages $V_F$ and $V_N$ of the two subsystems can be optimized to obtain a maximum power density $P^*_{max}$. Because the power output of the coupling system is mainly delivered by the SOFC, the efficiency $\eta_F$ is a monotonic increasing function of $V_F$, and thus, one can only optimize $V_N$ to obtain a local maximum efficiency for a given $V_F$, while $\eta$ increases monotonically
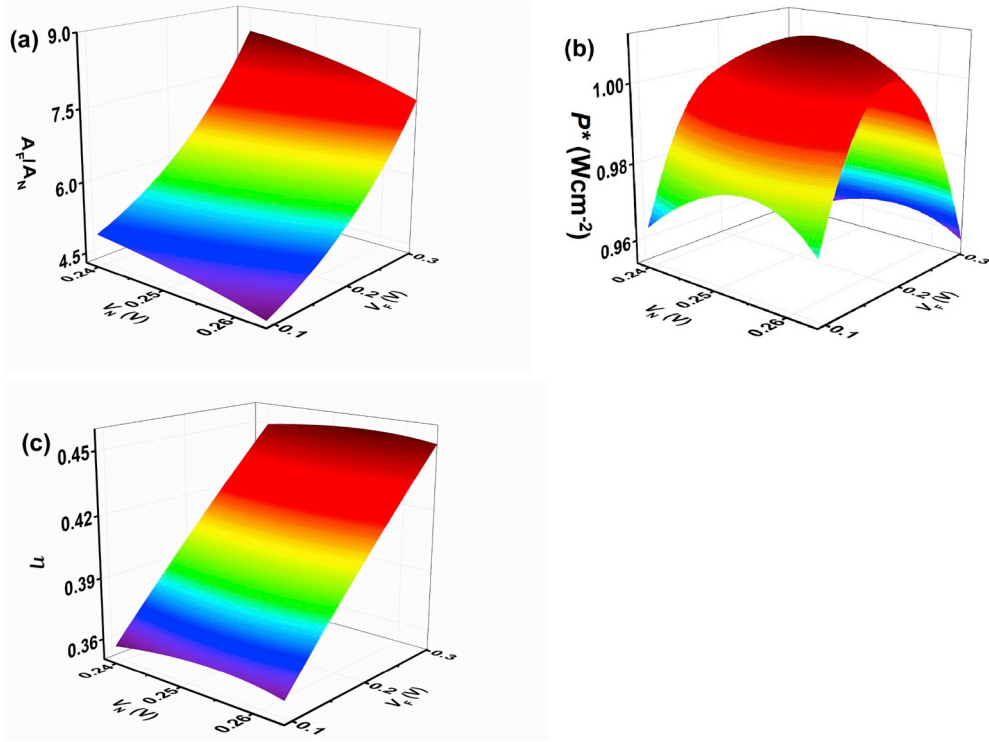
**Fig. 2.** Three-dimensional graphs of (a) the area ratio $A_F/A_N$, (b) the power output density $P^* = P/A_F$, (c) the efficiency $\eta$ varying with $V_F$ and $V_N$, where $\hbar\omega_g = E_g = 0.36$ eV and $d = 100$ nm.

with increasing $V_F$, as verified in Fig. 2(c).

In order to determine to optimal work regions, the curves of $P^*$, $P_F^*$, $\eta_F$, and $\eta$ as a function of $J_F$ are shown in Fig. 3, where the parameters $A_F/A_N$, $V_F$, $V_N$, and $J_N$ have been optimized. In Fig. 3(a), $J_{F,P}$ and $(A_F/A_N)_P$ are the values of $J_F$ and $A_F/A_N$ at the maximum power output density $P_{max}^*$, $J_{F,ub}$ and $(A_F/A_N)_{lb}$ are the upper bound current density and the lower bound area ratio, $J_{F,lb}$ and $(A_F/A_N)_{ub}$ are the lower bound current density and the upper bound area ratio when the power output density $P^*$ of the coupled system is equal to the maximum power output density $P_{F,max}^*$ of the SOFC. Fig. 3(a) shows that only when $J_F$ is located in the region $J_{F,su} < J_F \leq J_{F,ub}$, can the coupled system work normally. It is clearly observed from Fig. 3(a) that $P^*$ is not a monotonic function of $J_F$ and $A_F/A_N$, and consequently, there exists a maximum power output density $P_{max}^* = 1.01$ Wcm$^{-2}$. According to Eq. (15) and the values $(A_F/A_N)_P = 5.63$ and $J_{F,P} = 1.95$ Acm$^{-2}$, the optimal value $V_{F,P} = 0.180$ V and $V_{N,P} = 0.255$ V can be obtained. In Fig. 3(b), $\eta_{ub}$ is the upper efficiency when $J_F = J_{F,su}$ and $P^* = P_{F,max}^*$; $\eta_P$ is the efficiency when $P^* =$

$P_{max}^*$. The calculated result $(P^* - P_{F,max}^*)/P_{F,max}^* = 79.8\%$ indicates that the power output density has been significantly improved. Fig. 3 shows that the efficiencies of the single SOFC operated in the region of $J_F < J_{F,su}$ are larger than the efficiencies of the coupled system operated in the region of $J_{F,su} < J_F \leq J_{F,ub}$. However, the power output density is very small in the region of $J_F < J_{F,su}$. Obviously, when $J_{F,su} < J_F < J_{F,lb}$, although the power output density $P^*$ of the coupled system is smaller than $P_{F,max}^*$ of the SOFC, the efficiency of the coupled system in this range is significantly greater than the efficiency of the maximum power density point for the single SOFC system. Meanwhile, the power density and efficiency of the coupled system in this range are improved compared to the single SOFC system, and consequently, the coupled system operating in such a region is significant. When $J_{F,P} < J_F < J_{F,ub}$ and $(A_F/A_N)_P > A_F/A_N > (A_F/A_N)_{lb}$, $P^* > P_{F,max}^*$, both the efficiency and the power output density of the coupled system decrease with the increasing $J_F$, and the coupled system cannot be allowed to operate in this region. Thus, the optimal regions of $J_F$ and $A_F/A_N$ should be
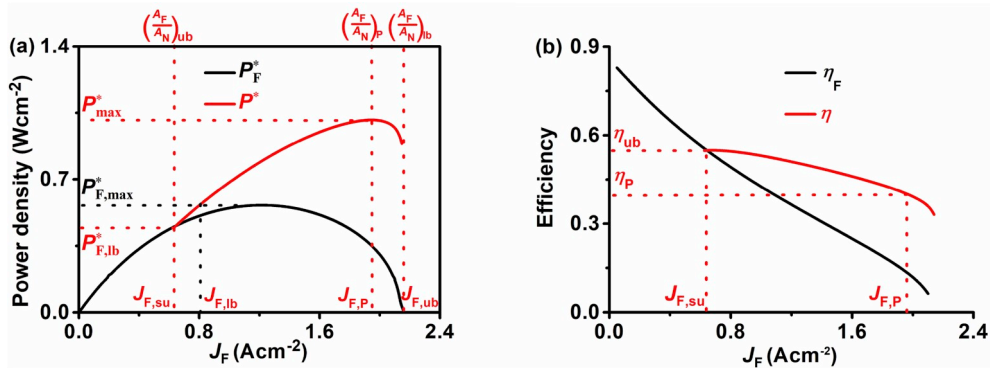


**Fig. 3.** The curves of (a) $P^*$ and $P_F^* = P_F/A_F$ and (b) $\eta$ and $\eta_F$ varying with $J_F$.

$$J_{F,su} < J_F \leq J_{F,P} \tag{19}$$

and

$$(A_F/A_N)_{ub} > A_F/A_N \geq (A_F/A_N)_P \tag{20}$$

According to the in equations (19) and (20), the power output density and the efficiency of the coupled can be determined as

$$P_{max}^* \geq P^* > P_{F,lb}^* \tag{21}$$

and

$$\eta_{ub} > \eta \geq \eta_P \tag{22}$$

The effects of the vacuum gap $d$ on the maximum power output density and the optimum operating conditions of the coupled system are shown in Fig. 4. It is seen from Fig. 4(a) that $(A_F/A_N)_P$ monotonically decreases with increase of $d$, because the enhancement of $A_N$ based on the photon tunneling effect is not significant as the NFTC with a large $d$. Fig. 4(a) displays that $P_{max}^*$ firstly decreases, and then increases as $d$ transition from near-field to far-field, finally changes negligibly with increase of $d$. The maximum power density in the near-field is 1.3 times than that in the far-field. The result indicates that integrating NFTC with the SOFC to form the coupled system is significant for enhancing the overall system efficiency. The variations of $V_{F,P}$ and $V_{N,P}$ with $d$ depend on the relations $P_{max}^* \sim d$ and $(A_F/A_N)_P \sim d$. Because the emitter radiates the photons flow and the heat flow towards the PV cell from the near-field to the far-field, and thus, the curves of $(A_F/A_N)_P$, $V_{F,P}$ and $V_{N,P}$ varying with $d$ are not smooth, as shown in Fig. 4(b). It is worthy for mentioning that Fig. 4(a) doesn't indicated that the performances can be greatly improved as the vacuum gap is decreased to nanoscale, because the new physical mechanisms may impact the operating of the NFTC, and consequently, the theory of fluctuation electrodynamics at the extreme near-field regions should be developed.

When the vacuum gap is sufficiently larger than the characteristic wavelength of thermal radiation given by Wien's displacement law, i.e., the far-field limit condition, the simplified heat flow $q_N$ and current density $J_N$ are, respectively, expressed as [34,35].

$$q_N = \frac{A_N}{4\pi^2\hbar^2c^3} \int_0^\infty \left[ \frac{E^3}{\exp[E/(KT_R)]-1} - \frac{E^3}{\exp[(E-V_Ne)/(KT_N)]-1} \right] dE \tag{23}$$

and

$$J_N = \frac{e}{4\pi^2\hbar^2c^3} \int_{E_g}^\infty \left[ \frac{E^2}{\exp[E/(KT_R)]-1} - \frac{E^2}{\exp[(E-V_Ne)/(KT_N)]-1} \right] dE \tag{24}$$

By re-writing Eqs. (23) and (24), the maximum power density $P_{max}^* = 0.755$ Wcm$^{-2}$ and the corresponding conditions $(A_F/A_N)_P = 5.29$, $V_{F,P} = 0.295$ V, and $V_{N,P} = 0.249$ V can be calculated. Combining the calculated result and Fig. 4(a), one can find that $P_{max}^*$, $(A_F/A_N)_P$, and $V_{N,P}$ of the near-field coupled system are larger than that of the far-field coupled system, whereas the optimum value $V_{F,P}$ of the near-field coupled system is smaller than the that of the far-field coupled system. As the photon tunneling effect in the far-field regime can be neglected, the radiative heat flow and the current density are not enhanced. The far-field coupled system needs a small value $(A_F/A_N)_P$ to meet the thermal balance equation, i.e., Eq. (15).

## 4. Discussion

Table 2 shows that $V_{F,P}$, $P_{max}^*$, $\eta_{ub}$, and $\eta_P$ are not a monotonic function of $T_F$ when $T_F$ varies in the range of 873–1273 K. Further, one can find that $(A_F/A_N)_P$ and $V_{N,P}$ increase as $T_F$ is increased. Table 2 depicts that $P_{max}^*$ is a monotonically decreasing function of $T_F$ as the SOFC operates at especial temperature regions, because the black-body radiation heat loss and the NFRHT $q_N$ increase as $T_F$ is increased, the coupled system must increase the area $A_F$ to meet the energy balance Eq. (15), and thus, the power density is decreased. An objective function $Z = P_{max}^* \times \eta_{ub}$ is introduced to make a trade-off between the power density and the efficiency. One can discover that there exists a maximum value of $Z$ and the corresponding optimum $T_F$. The result indicates that the temperature $T_F$ is of great importance for the design of the coupling system. By using the regenerator, the SOFC temperature can be adjusted to approach the optimum temperature.

In order to expound that the performance of the coupled system mentioned here is better than that of other SOFC-based coupled systems, we calculate the maximum power densities $P_{max}^*$ of the coupled system operated at several temperatures $T_F$ (e.g., 873 K, 1073 K, 1173 K, and 1273 K), as shown in Fig. 5(a). The curve connected by these points in Fig. 5(a) can be used to indicate the maximum power output densities of the SOFC-NFTC coupled system operated in the normal operating temperature range of SOFC. For the convenience of comparison, the maximum power output densities $P_{max}^*$ of other SOFC-based coupled systems operated at different temperatures $T_F$ are marked on Fig. 5(a). In addition to SOFC-gas turbine and SOFC-Brayton coupled systems, the maximum power output densities of the coupled system mentioned here are larger than those of other SOFC-based coupled systems. More importantly, the SOFC-NFTC coupled system owns the advantages of small-size, simple design, low noise, easy maintenance, etc. and consequently, theoretical simulation on the SOFC-NFTC coupled system is very significant and the experimental investigation including the optimum matching of two subsystems can be easily carried out.

**Table 2**
The key parameters of the SOFC-NFTC coupling system with varying $T_F$, where $d = 100$ nm.

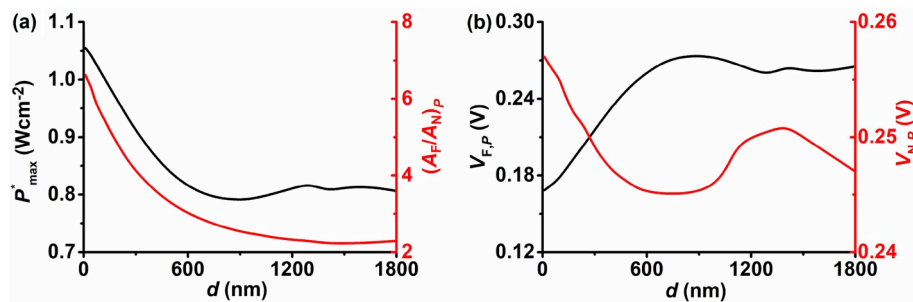| $T_F$ (K) | $V_{F,P}$ (V) | $V_{N,P}$ (V) | $(A_F/A_N)_P$ | $P_{max}^*$ (Wcm$^{-2}$) | $\eta_{ub}$ | $\eta_P$ |
|---|---|---|---|---|---|---|
| 873 | 0.158 | 0.225 | 2.59 | 0.647 | 0.542 | 0.340 |
| 1073 | 0.180 | 0.255 | 5.63 | 1.01 | 0.548 | 0.402 |
| 1173 | 0.252 | 0.266 | 9.55 | 1.13 | 0.532 | 0.439 |
| 1273 | 0.127 | 0.276 | 11.6 | 0.742 | 0.341 | 0.301 |



**Fig. 4.** The curves of (a) $P_{max}^*$ and $(A_F/A_N)_P$ of the coupled system and (b) $V_{F,P}$ and $V_{N,P}$ varying with the vacuum gap $d$.
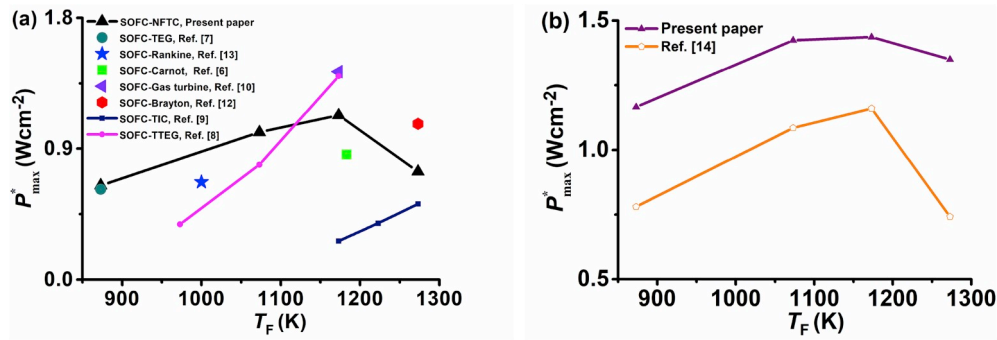
**Fig. 5.** The comparison of the maximum power output densities of various SOFC-based coupled systems – (a) comparsion with various systems from the literature; (b) comparison with a particular reference [14].

In addition, one can find that the maximum power densities of Ref. [14] are larger than those of the present work. The mechanisms are explained as follows. Firstly, the convection heat-leak from the SOFC is taken into account in Ref. [14], while the black-body thermal radiation loss from the SOFC is considered in this work. Secondly, the sub-bandgap photons are reflected back to the radiator by means of the back surface reflector (BSR), while the sub-bandgap photons contributed to the NFRHT is considered. Thirdly, the two different III-V group semiconductors InGaAsSb (0.40 eV) and InAs (0.36 eV) are, respectively, chosen to make the PV cells in Ref. [14] and this work. As a result, the energy losses in this work are larger than Ref. [14], and thus, the maximum power densities in this work are smaller than those in Ref. [14].

In order to conveniently make comparisons, we select the same InAs semiconductor material and consider the black-body radiation loss to calculate $P^*_{\mathrm{max}}$ of the SOFC-FFTC system, as shown in Fig. 5(b). Further, the BSR is placed at the bottom of the PV cell to recalculate $P^*_{\mathrm{max}}$ of the SOFC-NFTC system, as shown in Fig. 5(b). One can find that the maximum power output densities of the SOFC-NFTC system are larger than those of SOFC-FFTC system. The results indicate that the improvement of the SOFC-NFTC system by means of the NFRHT and the BSR is significant.

## 5. Conclusions

A new energy system consisting of an SOFC and a NFTC has been proposed and theoretically evaluated. The main results are listed as follows:

(1) According to the energy balance equation, the relations between the output voltages of the subsystems and the area ratio of the SOFC to the NFTC are revealed, and the start-up current density of the SOFC is numerically determined.

(2) The performance characteristics of the SOFC-NFTC coupled system are studied by numerically. The maximum power output density $P^*_{\mathrm{max}} = 1.01\,\mathrm{Wcm}^{-2}$ and the corresponding optimum conditions $(A_{\mathrm{F}}/A_{\mathrm{N}})_{\mathrm{P}} = 5.63$, $J_{\mathrm{F,P}} = 1.95\,\mathrm{Acm}^{-2}$, $V_{\mathrm{F,P}} = 0.180\,\mathrm{V}$, and $V_{\mathrm{N,P}} = 0.255\,\mathrm{V}$ are obtained. By comparing to the single SOFC, the power output density is increased by 79.3%, and the optimally working regions of key parameters are presented as Eqs. (19)-(21). The effects of the NFTC's vacuum gap on the optimum performance of the coupled system are discussed.

(3) The far-field performance limit of the coupled system is studied. The results reveal that the coupled system operated at near-field regime is better than it operated at far-field regime.

(4) The maximum power output densities of the SOFC-NFTC coupled system operated at different temperatures are compared with those of other SOFC-based coupled systems.

In summary, the results obtained in present work show that the SOFC-NFTC coupled systems have some advantages over other SOFC-based coupled systems and are worth to be further investigated.

## Declaration of competing interest

The authors declare that they have no known competing financial interests or personal relationships that could have appeared to influence the work reported in this paper.

## References

[1] P. Boldrin, N.P. Brandon, Nature Catalysis 2 (2019) 571.
[2] C. Bao, Z. Jiang, X. Zhang, J. Power Sources 294 (2015) 317–332.
[3] M. Ni, Int. J. Hydrogen Energy 37 (8) (2012) 6389–6399.
[4] M. Ni, J. Power Sources 202 (2012) 209–216.
[5] K. Huang, S.C. Singhal, J. Power Sources 237 (2013) 84–97.
[6] Y. Zhao, J. Chen, J. Power Sources 186 (2009) 96–103.
[7] X. Chen, Y. Pan, J. Chen, Fuel Cell 10 (2010) 1164–1170.
[8] H. Zhang, W. Kong, F. Dong, H. Xu, B. Chen, M. Ni, Energy Convers. Manag. 148 (2017) 1382–1390.
[9] Y. Wang, L. Cai, T. Liu, J. Wang, J. Chen, Energy 93 (2015) 900–907.
[10] X. Zhang, Y. Wang, T. Liu, J. Chen, Energy Convers. Manag. 86 (2014) 1102–1109.
[11] X. Chen, B. Lin, J. Chen, Energy Fuels 23 (2009) 6079–6084.
[12] E. Açıkkalp, Energy Convers. Manag. 148 (2017) 279–286.
[13] D.F. Waters, Christopher P. Cadou, J. Power Sources 221 (2013) 272–283.
[14] T. Liao, L. Cai, Y. Zhao, J. Chen, J. Power Sources 306 (2016) 666–673.
[15] R. Messina, P. Ben-Abdallah, Sci. Rep. 3 (2013) 1383.
[16] A. Datas, R. Vaillon, Nano Energy 61 (2019) 10–17.
[17] A. Datas, R. Vaillon, Appl. Phys. Lett. 114 (2019) 133501.
[18] T. Liao, X. Zhang, X. Chen, J. Chen. J. Appl. Phys. 125 (2019), 203103.
[19] M.P. Bernardi, D. Milovich, M. Francoeur, Nat. Commun. 7 (2016) 12900.
[20] B. Song, D. Thompson, A. Fiorino, Y. Ganjeh, P. Reddy, E. Meyhofer, Nat. Nanotechnol. 11 (2016) 509–514.
[21] A. Fiorino, D. Thompson, L. Zhu, B. Song, P. Reddy, E. Meyhofer, Nano Lett. 18 (2018) 3711.
[22] A. Fiorino, L. Zhu, D. Thompson, R. Mittapally, P. Reddy, E. Meyhofer, Nat. Nanotechnol. 13 (2018) 806–811.
[23] D.A. Noren, M.A. Hoffman, J. Power Sources 152 (2005) 175–181.
[24] F. Calise, A. Palombo, L. Vanoli, J. Power Sources 158 (2006) 225–244.
[25] C. Wang, M.H. Nehrir, S.R. Shaw, IEEE Trans. Energy Convers. 20 (2005) 442–451.
[26] Y. Ji, K. Yuan, J.N. Chung, Y.C. Chen, J. Power Sources 161 (2006) 380–391.
[27] H. Zhu, R.J. Kee, J. Power Sources 117 (2003) 61–74.
[28] S.J. Watowich, R.S. Berry, J. Phys. Chem. 90 (1986) 4624–4631.
[29] H.R. Xu, B. Chen, P. Tan, W.Z. Cai, D. Farrusseng, M. Ni, Appl. Energy 219 (2018) 105–113.
[30] T. Liao, Z. Yang, Q. Dong, X. Chen, J. Chen, IEEE Trans. Electron. Dev. 64 (2017) 4144–4148.
[31] T. Liao, Z. Yang, W. Peng, X. Chen, J. Chen, Energy Convers. Manag. 152 (2017) 214–220.
[32] P. Würfel, J. Phys. C Solid State Phys. 15 (1982) 3967–3985.

[33] E. Tervo, E. Bagherisereshki, Z. Zhang, Front. Energy 12 (2018) 5–21.

[34] X. Zhai, J. Lai, H. Liang, S. Chen, J. Appl. Phys. 108 (2010), 074507.

[35] P.F. Baldasaro, J.E. Raynolds, G.W. Charache, D.M. DePoy, C.T. Ballinger, T. Donovan, J.M. Borrego, J. Appl. Phys. 89 (2001) 3319.